TUDelft

Delft University of Technology

Prediction of the In-Plane Response of Masonry Walls Using a Piecewise Softening Contact Model Within the Distinct Element Method

Oktiovan, Yopi; Messali, Francesco; Lemos, José; Pulatsu, Bora; Rots, Jan

Important note
To cite this publication, please use the final published version (if applicable).
Please check the document version above.

Prediction of the In-Plane Response of Masonry Walls Using a Piecewise Softening Contact Model Within the Distinct Element Method

Yopi Oktiovan[1]([✉]) , Francesco Messali[1] , José Lemos[2] , Bora Pulatsu[3] , and Jan Rots[1]

[1] Faculty of Civil Engineering and Geosciences, Delft University of Technology, 2628CN Delft, Netherlands
y.p.oktiovan@tudelft.nl
[2] National Laboratory for Civil Engineering (LNEC), Lisbon, Portugal
[3] Department of Civil and Environmental Engineering, Carleton University, K1S 5B6 Ottawa, Canada

Abstract. Masonry structures, integral components of architectural heritage, are diffuse worldwide and continue to be interwoven within modern infrastructures. The complex nature of their constituents has driven active research toward understanding their mechanical behavior. Accurately and robustly representing the nature of masonry constituents is essential for structural analysis, design, and preservation tasks. This study adopts an adjustable contact constitutive model recently proposed to simulate bond behavior in masonry assemblages subjected to in-plane shear-compression loading. The adopted contact constitutive model, recently proposed by the authors within the Distinct Element Method (DEM) framework, addresses the intricate behavior of unit-mortar interfaces by employing a piecewise linear softening function controlled by the user to capture the softening regime in tension and shear. Meanwhile, the compressive region of the masonry interfaces is controlled by a compressive cap with a radial return algorithm under the explicit time-marching integration scheme of DEM to implicitly couple the shear and compressive behavior. The performance of the constitutive model was assessed on a set of calcium silicate wall experiments tested under in-plane shear and compression loading and presented a comprehensive variety of failure modes. The experimental and numerical results are compared on each system's global and local behaviors. The findings underscore the robustness of the proposed contact constitutive model in accurately capturing the complex mechanical response of masonry and highlight its potential for structural analysis and damage prediction of a diverse spectrum of masonry structures.

Keywords: Masonry · Distinct element method · Contact constitutive model · Piecewise linear softening · Multi-surface plasticity · In-plane shear-compression tests

1 Introduction

Unreinforced masonry (URM) structures are recognized as one of the earliest human-made constructions because of their remarkable capacity to endure gravitational forces, cost efficiency, and straightforward construction process. It is also generally known that URM structures are susceptible to damage due to significant lateral loads, such as strong wind or earthquake loads. Considering this, the study of the mechanical properties of URM structures has consistently been a prominent area of research despite the declining global use of URM structures caused by the emergence of more modern construction materials, such as reinforced concrete and steel.

In recent decades, with the increase in computational power, numerous numerical modeling techniques have been proposed to investigate the mechanical behavior of URM structures. These techniques vary in modeling complexity and the tradeoff between computational time and prediction accuracy. The computational modeling of masonry structures is largely categorized into three groups [8]: Macro-modeling approaches [1,11,13] where masonry is assumed as a continuum body with no separation between masonry units and mortar joints so the discrete nature of masonry is represented by either calibrated constitutive models or homogenized procedures; Simplified micro-modeling approaches [2,4,6] where bricks are continuum elements and mortar joints are defined as zero-thickness interfaces where the system nonlinearity is lumped. and Detailed micro-modeling approaches [3,14,15] where brick units, mortar layers, and the interfaces between them are modeled separately. The numerical strategy proposed in this research follows the simplified micro-modeling approach as it balances the modeling simplicity offered by the macro-modeling approaches and the increased accuracy and representation of localized damage in the detailed micro-modeling approaches.

This paper adopts a novel contact constitutive model, recently introduced by the authors [10], to be utilized in a distinct element method (DEM) framework within the simplified micro-modeling strategy to simulate a set of calcium silicate masonry walls tested under in-plane shear-compression loading conditions. The contact constitutive model includes the multi-surface plasticity concept by Lourenço and Rots [7] with damage evolution law. The contact model is adjustable as user-defined piecewise linear softening functions are used on the tension and shear post-peak regimes, while hardening/softening law is defined for the compression regime.

Numerical simulations of URM walls subjected to shear-compression loading under different boundary conditions and shear ratios are conducted to demonstrate the capability of the constitutive model under DEM in simulating the complex responses of URM structures.

2 Brief Background of the Distinct Element Method

The contact constitutive model in this paper is developed within the DEM framework, which uses the explicit time-marching integration solver to obtain equilibrium within the equations of motion. Under DEM, the units can be modeled as

rigid or deformable blocks with linear elastic laws. The nodal displacement at node point i is obtained via a simple equation shown in Eq. (1).

$$u_i^{t^+} = u_i^{t^-} + \dot{u}_i^{t^+} \cdot \Delta t \tag{1}$$

where u^{t^+} and u^{t^-} are the displacements at $t + \Delta t/2$ and $t - \Delta t/2$, respectively, Δt is the time increment, and $\dot{u}_i^{t^+}$ is the nodal velocity vector at $t + \Delta t/2$, obtained through the equation of motion in Eq. (2). This is defined according to the finite difference form of Newton's second law of motion.

$$\dot{u}_i^{t^+} = \dot{u}_i^{t^-} + \left(\Sigma F_i^{(t)} - F_{d,i} \right) \frac{\Delta t}{m} \tag{2}$$

where $\dot{u}_i^{t^-}$ is the nodal velocity vector at the time $t - \Delta t/2$, m is the nodal mass, $\Sigma F_i^{(t)}$ is the total force, and $F_{d,i}$ is the nodal damping force, defined in Eq. (3).

$$F_{d,i} = \alpha |\Sigma F_i^{(t)}| sgn(\dot{u}^{t^-}) \tag{3}$$

The damping force is based on a proportion of the total force, controlled by a non-dimensional damping constant α set equal to 0.8, and the direction of the velocity vector (owned by the sign function). Meanwhile, the total force $\Sigma F_i^{(t)}$ is defined in Eq. (4).

$$F_i = F_i^z + F_i^c + F_i^l + F_i^g \tag{4}$$

where F_i^z is the force due to internal stress at the deformable blocks, F_i^c force at the contact point, F_i^l is the external load, and F_i^g is the gravitational force.

The force at the contact point F_i^c in Eq. (4) exists only at the nodal points of the block that are in contact with the other blocks, i.e. along the block boundary. This force is zero at nodal points outside the block boundary. The contact force F_i^c is formulated in Eq. (5).

$$F^c = F_n \cdot \mathbf{n} + \sum_{j=1}^{2} F_{s,j} \tag{5}$$

where $\mathbf{n}$ is the unit normal vector towards the contacting bodies, F_n and F_s are the normal and shear force vectors, respectively. The normal and shear force vectors are respectively formulated in Eqs. (6), (7).

$$F_n := F_n + \Delta F_n \ \text{ where } \ \Delta F_n = k_n \cdot \Delta U_n \cdot A_c \tag{6}$$

$$F_{s,j} := F_{s,j} + \Delta F_{s,j} \ \text{ where } \ \Delta F{s,j} = k_s \cdot \Delta U_{s,j} \cdot A_c \tag{7}$$

where the superscript j denotes the two shear directions ($j = 1, 2$), k_n and k_s are the normal and shear stiffnesses, respectively, ΔU_n and $\Delta U_{s,j}$ are the normal and shear displacement increments, respectively, and A_c is the subcontact area, calculated as $1/3$ of the triangular faces' areas where the subcontact lies.

At each timestep, the law of motion in Eq. (2) is applied, and the subcontact force-displacement relations are defined. The integration of the equation of motion gives new block positions and the contact displacement increments (Eq. (1). The subcontact force-displacement law (Eqs. (6), (7) under linear elastic condition) is then implemented to obtain new subcontact forces, which are then applied to Eq. (4) and subsequently Eq. (2). This cycle is repeated until either equilibrium or failure is achieved. The latter refers to the condition where the evaluated node is unable to find a steady-state flow as it accelerates to infinity.

3   Contact Constitutive Model

The forces at the contact points behave as indicated in Eq. (5) under the linear elastic law. If elastoplastic laws are implemented to the contact points, the force vector needs to be corrected to limit the failure load specified by the applied contact laws. The contact constitutive law that is typically used for masonry structures within the DEM framework is the Coulomb slip contact model.

In this model, the shear and normal stresses in tension develop according to the linear elastic law until the stresses reach the peak strength. Upon damage in each regime, the shear strength drops to the residual strength while the tensile strength drops to zero. It is clear that this model provides a brittle representation of the unit-mortar interfaces, which is sufficient in predicting the ultimate capacity of masonry structures. In reality, post-peak softening does occur in masonry structures in tension and shear regimes [5]. Furthermore, the Coulomb slip model assumes an infinite strength in the compression regime, whereas, in reality, compressive crushing at both unit and mortar does occur on masonry structures subjected to high axial stress or higher aspect ratio.

The novel contact constitutive model proposed in this paper utilizes the multi-surface plasticity combined with the damage mechanics to address the mechanical behavior of masonry constituents in tension, shear, and compression. This constitutive model is developed within the DEM framework under the small displacement theory, where no new contacts are generated throughout the numerical simulation. This is done to avoid unreasonable contact interpenetration upon compressive crushing at the unit-mortar interfaces.

The proposed contact model utilizes the multi-surface plasticity model, presented in Fig. 1. The yield function consists of three surfaces: a tension cut-off region represented by F_1, the Coulomb-slip region defined in F_2, and an elliptical curve as a compression 'cap' to control the shear-compression in F_3. The mathematical functions for the yield surfaces are shown in Eq. (8).

$$F_1 = \sigma - f_t(u_n^t) \tag{8a}$$

$$F_2 = |\tau| + \sigma \tan \phi(u_s) - f_s(u_s) \tag{8b}$$

$$F_3 = C_{nn}\ \sigma^2 + Css\ \tau^2 + C_n\ \sigma - f_c^2(u_n^c) \tag{8c}$$

where u_n^c and u_n^t are the relative normal subcontact displacement in compression and tension, respectively, σ is the normal stress, τ is the shear stress, $\phi(u_s)$ is the
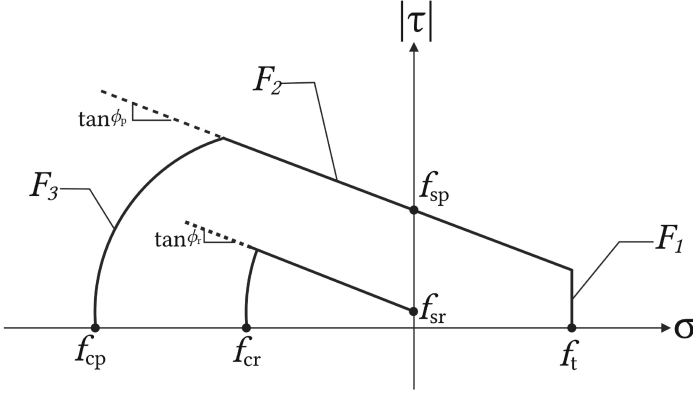
Fig. 1. Two-dimensional yield surfaces in normal stress vs shear stress space

friction angle correlated to the shear displacement, $f_t(u_n^t)$ is the tensile strength that evolves in accordance with the positive normal displacement, $f_s(u_s)$ is the cohesive strength correlated to the shear displacement, $f_c(u_n^c)$ is the compressive strength that evolves in accordance with the negative normal displacement, C_{nn}, C_{ss}, and C_n are the controlling parameter of the compression cap in Fig. 1.

An associated flow rule is implemented for F_1 and F_3, while the non-associated flow rule is used for the F_2 yield surface to address the dilatancy of the mortar joints upon shear damage [16]. The mathematical function of the plastic potential G_2 is presented in Eq. (9).

$$G_2 = |\tau| + \sigma \tan\psi - f_s(u_s) \tag{9}$$

where ψ is the dilatancy angle.

The strength degradation of the contact points at the onset of damage is controlled by damage parameters corresponding to damage in tension (d_t), shear (d_s), and compression (d_c). A similar approach to Pulatsu [12] is considered where the tension and shear softening are coupled. This is achieved by combining the damage parameters in shear and tension into a combined damage parameter d_{ts} defined in Eq. (10).

$$d_{ts} = d_t(\bar{u}_n) + d_s(\bar{u}_s) - (d_t(\bar{u}_n)d_s(\bar{u}_s)) \tag{10}$$

The post-peak softening of the tensile strength is given in Eq. (11), where f_t is the peak tensile strength.

$$f_t(u_n^t) = f_t(1 - d_{ts}) \tag{11}$$

The tensile damage parameter $d_t(u_n^c)$ in Eq. (10) is a user-defined value that depends on the normal displacement ratio, defined in Eq. (12).

$$\bar{u}_n = \frac{u_n^t}{u_{np,t}} \quad \text{where} \quad u_{np,t} = \frac{f_t}{k_n} \tag{12}$$

The tabulated values provided by the users are the table of pairs $(\bar{u}_n, d_t)$, where $\bar{u}_n$ begins at 1 at the peak and decreases to zero at the residual state, while d_t starts at zero at the peak and increases to 1 at the residual state. The tabulated values allow users to approximate any given shapes of the post-peak softening curve in tension through a piecewise linear function.

The formulation in shear is similar to the tension, where the shear displacement ratio controls the shear damage parameter $d_s(\bar{u}_s)$ in Eq. (10), shown in Eq. (13).

$$\bar{u}_s = \frac{u_s}{u_{sp}} \tag{13}$$

where u_{sp} is the displacement at peak shear strength, defined in Eq. (14).

$$u_{sp} = \frac{\tau_p}{k_s} \tag{14}$$

where τ_p is the peak shear strength defined in Eq. (15).

$$\tau_p = c_p - \sigma \tan(\phi_p) \tag{15}$$

where c_p and ϕ_p are the peak cohesion strength and friction angle, respectively.

The post-peak shear strength is formulated according to the Mohr-Coulomb envelope where the cohesion c and the friction angle depend on a user-defined shear damage parameter d_s, as shown in Eq. (16).

$$\tau(\bar{u}_s) = c(\bar{u}_s) - \sigma \tan(\phi)(\bar{u}_s) \tag{16}$$

where $c(\bar{u}_s)$ and $\tan(\phi)(\bar{u}_s)$ are the post-peak cohesion and friction angle, respectively, formulated in Eq. (17).

$$c(\bar{u}_s) = c_r + (c_p - c_r)(1 - d_{ts}) \tag{17a}$$

$$\tan(\phi)(\bar{u}_s) = \tan(\phi_r) + (\tan(\phi_p) - \tan(\phi_r))(1 - d_{ts}) \tag{17b}$$

Similar to the tension regime, the shear damage parameter is defined by a table of pairs $(\bar{u}_s, d_s)$ where $\bar{u}_s$ starts at 1 at peak and reduces to zero at residual state while d_s starts at zero at peak and increases to 1 at residual state.

Finally, the behavior of the contact model in compression is controlled by a hardening/softening law. The hardening phase starts after the initial linear-elastic phase, typically observed between 30% to 40% of the compressive strength. The hardening phase is defined by a parabolic function shown in Eq. (18).

$$\sigma_c(u_n^c) = \sigma_{el} + (f_{cp} - f_{c;el})\sqrt{\frac{2u_{inel}}{u_{cp}} - \frac{u_{inel}^2}{u_{cp}}} \tag{18}$$

where $\sigma_c(u_n^c)$ is the current compressive stress during the hardening phase, $f_{c;el}$ is the elastic compressive stress (set at 30% of the compressive strength by default), f_{cp} is the peak compressive strength, u_{cp} is the normal compressive

displacement at peak compressive strength and u_{inel} is the inelastic normal compressive displacement.

The inelastic displacement is the irrecoverable displacement calculated as the total joint displacement (u_n^c) subtracted by the displacement at elastic compressive stress. The peak compressive displacement is formulated in Eq. (19), which is controlled by a non-dimensional parameter n, the factor of the supposed displacement at peak compressive strength under the initial stiffness.

$$u_{cp} = n \cdot \frac{f_{cp}}{k_n} \tag{19}$$

The compressive damage is assumed to be initiated after the peak compressive strength is reached. The current compressive strength $\sigma_c(u_n^c)$, after peak strength is reached, is shown in Eq. (20).

$$\sigma_c(u_n^c) = (1 - d_c) \cdot f_{cp} \tag{20}$$

The compressive damage parameter d_c in Eq. (20) is based on the implementation by Lourenço and Rots [7], defined in Eq. (21).

$$d_c = \begin{cases} 0, & u_n^c < u_{c,p} \\ \left(1 - \frac{f_{cm}}{f_{cp}}\right)\left(\frac{u_n^c - u_{cp}}{u_{cm} - u_{cp}}\right)^2 & u_{cp} \leq u_n^c < u_{cm} \\ \left(1 - \frac{f_{cr}}{f_{cp}}\right) - \frac{f_{cm} - f_{cr}}{f_{cp}}\exp\left(\alpha\frac{u_n^c - u_{cm}}{f_{cm} - f_{cr}}\right) & u_n^c \geq u_{cm} \end{cases} \tag{21}$$

where f_{cm} is the intermediate compressive stress between peak and residual compressive strength, defined as the point of inflection from quadratic to exponential softening, f_{cr} is the residual compressive strength, u_{cm} is the displacement at intermediate compressive strength, and α is the parameter defining the slope of the exponential function in Eq. (22).

$$\alpha = 2\frac{f_{cm} - f_{cp}}{u_{cm} - u_{cp}} \tag{22}$$

The intermediate compressive strength is fixed as the average value between peak and residual compressive strength. Similar to the displacement at peak compressive strength in Eq. (19), the displacement at intermediate compressive strength is controlled by a non-dimensional parameter m as a factor to the displacement at peak compressive strength, as defined in Eq. (23).

$$u_{cm} = m \cdot u_{cp} \tag{23}$$

where the non-dimensional parameter m is defined in Eq. (24).

$$m = \frac{G_c - 0.5\frac{f_{cp}^2}{9k_n} - 0.65(u_{cp} - u_{c;el})f_{cp} + 0.75\kappa + 0.25\xi}{\kappa + \xi} \tag{24}$$

where G_c is the compressive fracture energy, $u_{c;el}$ is the displacement at elastic compressive stress $f_{c;el}$, defined as $f_{c;el}/k_n$, κ and ξ are defined in Eq. (25).

$$\kappa = u_{cp}f_{cp} \quad \text{and} \quad \xi = u_{cp}f_{cr} \tag{25}$$

By correlating the m parameter to the compressive fracture energy, the fracture energy under the hardening/softening law can be approximated to that calculated based on the multi-linear softening law. The contact model is implemented in *3DEC*, the commercial software package for DEM, as a user-defined contact constitutive model. In the following section, this modeling strategy will be validated against an experiment on calcium silicate masonry walls subjected to shear-compression loading under different boundary conditions and shear ratios.

4   Numerical Simulations of Calcium-silicate Masonry Walls Subjected to In-Plane Shear-Compression Loading

The structural response of four walls with different shear ratios and boundary conditions from the experimental campaign reported by Messali et al. [9] is simulated to show the suitability of the proposed numerical modeling strategy to predict the performance of such type of structures. Two couples of calcium silicate (CS) squat and slender walls with double-clamped and cantilever configurations were selected. The CS walls were subjected to vertical pre-compression and quasi-static in-plane loads until the near-collapse condition was reached. However, the numerical modeling in this paper is limited to only monotonic in-plane loads. Hence, the global response in terms of the force-displacement curve is compared to the envelope curve from the experimental results, as well as the crack pattern.

4.1   Experimental and Numerical Setups

The geometrical properties of the walls are presented in Table 1. The masonry wall specimen comprises 34 courses of CS bricks with nominal dimensions of 210 × 71 × 102 mm (L × H × W) with 10mm of mortar layers. For the numerical simulation, the masonry unit is expanded to account for the zero-thickness interfaces representing the mortar joints. Therefore, the unit dimensions for the numerical simulation are set to 220 × 81 × 102 mm.

The experimental crack patterns observed at the end of the tests for the selected specimens are presented in Fig. 2. The behavior of the slender walls was mostly governed by a rocking mechanism with the opening of bed joints at the top and bottom corners of the wall for the double-clamped specimen (TUD-COMP-0a) and only the bottom corner for the cantilever specimen (TUD-COMP-1). The opening of the bed joints was then followed by short diagonal cracks that opened slightly close to the corners. After the peak load was achieved, splitting of the brick units and sliding along the bed joints occurred along with toe crushing, defining the failure mechanism of the slender walls.

Table 1. Geometrical properties of validated wall specimens [9]

Specimen name	Dimensions [m] $l_w \times h_w \times t_w$	Shear ratio	Boundary conditions	Vertical pre-compression [MPa]
TUD-COMP-0a	$1.1 \times 2.76 \times 0.102$	1.25	Double clamped	0.70
TUD-COMP-1	$1.1 \times 2.76 \times 0.102$	2.90	Cantilever	0.70
TUD-COMP-4	$4.0 \times 2.76 \times 0.102$	0.35	Double clamped	0.50
TUD-COMP-6	$4.0 \times 2.76 \times 0.102$	0.80	Cantilever	0.50

TUD-COMP-0a   TUD-COMP-4
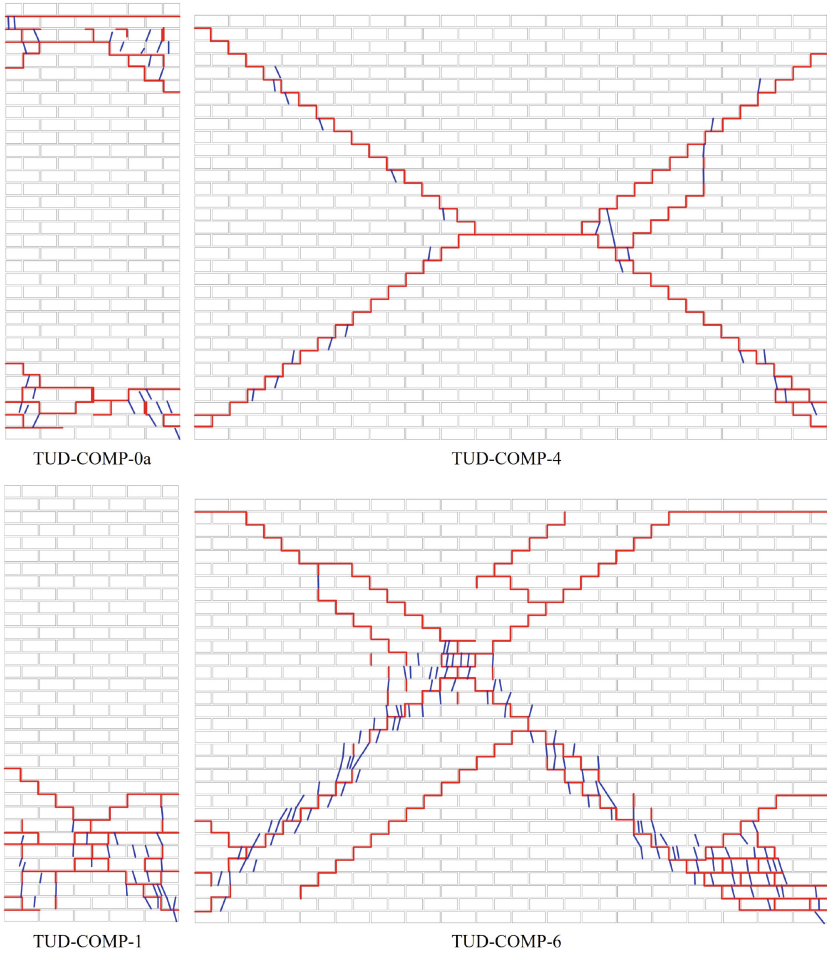
TUD-COMP-1   TUD-COMP-6

Fig. 2. Experimental crack pattern at the end of the tests [9]

Meanwhile, the behavior of the squat walls was governed by shear-dominated failure. For both cases of TUD-COMP-4 and TUD-COMP-6, the diagonal shear cracks initiated from regions close to the center and then propagated towards the corners of the walls. The diagonal cracks of the TUD-COMP-4 were apparent and localized without any change of inclination during each loading cycle. Meanwhile, the diagonal cracks of the TUD-COMP-6 specimen were more dispersed, with several diagonal cracks parallel to the main diagonal, followed by the splitting of the brick units along the diagonal cracks.

A single set of material properties was selected for all numerical simulations. The adopted values are listed in Table 2. The material properties are obtained from the material companion tests. The tensile strength, cohesive strength, and compression peak ratio of the interfaces were calibrated to match the global experimental responses.

Table 2. Material properties of the calcium silicate masonry walls

Properties	Symbol	Unit	Value	
			Bed joint	Head joint
Unit properties				
Modulus of elasticity	E_b	MPa	4800	
Poisson's ratio	v	[–]	0.16	
Density	ρ	kg m^{-3}	1800	
Interface properties				
Modulus of elasticity	E_u	MPa	3174	2212
Mortar compressive strength	f_m	MPa	6.59	
Mortar modulus of elasticity[a]	E_m	MPa	1973.7	
Tensile strength[b]	f_t	MPa	0.1	
Cohesive strength[b]	f_s	MPa	0.11	
Friction coefficient	μ	[–]	0.43	
Compressive strength	f_c	MPa	7.55	5.93
Compressive fracture energy	G_c	N m^{-1}	15000	31500
Peak ratio[a]	n	[–]	68.5	

[a]Value derived from equations reported in Jafari et al. [5]
[b]Values calibrated to match global experimental responses

The normal and shear stiffnesses, required for correlating the contact force and displacement in Eqs. (6), (7), respectively, are defined in Eq. (26) [8]. The stiffnesses are calculated from the properties of the masonry constituents and the joint thickness.

$$k_n = \frac{E_b E_m}{t_m(E_b - E_m)} \quad and \quad k_s = \frac{k_n}{2(1+v)} \tag{26}$$

where t_m is the mortar thickness, set to 10mm for this experimental validation.

The user-defined softening functions in shear and tension are defined by the exponential functions by Lourenço and Rots [7] divided into 200 segments. The post-peak softening behaviors are presented in Fig. 3. The scalars plotted in Fig. 3 are non-dimensional.

(a) d_s ratio   (b) d_t ratio
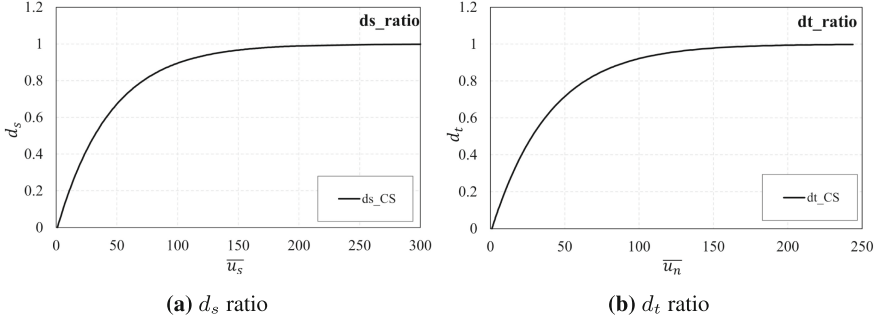
Fig. 3. Shear and tensile post-peak softening behaviors for the CS wall test

For all validated walls, the loads and supports are applied via blocks with high modulus of elasticity connected to the wall models with linear elastic contact law. The block discretization of the model for slender and squat walls is shown in Fig. 4. For the sake of simplicity, only the representative model is presented in Fig. 4, i.e. TUD-COMP-1 and TUD-COMP-4 for the cantilever-slender and double-clamped-squat walls, respectively. For the walls with the cantilever configuration, the in-plane rotation of the top 'rigid' block is freed, with the block height extended to the point where zero moment is observed according to the wall shear ratio. This is to ensure that the applied lateral load imposed the correct amount of moment at the wall base.

For the walls with the double-clamped configuration, the in-plane rotation of the top block is fixed, and since the location of the applied load does not matter in this case, the height of the top block is equal to the bottom block. The loading sequence is the same for both cantilever and double-clamped configurations. The wall system is first brought to equilibrium under gravity load. The pre-compression load is then applied as distributed loads at the top surface of the top block, and the equilibrium is solved again. Once stabilized, the lateral load is applied as velocity with a constant rate of 1mm s^{-1}.

The velocity is only applied at the nodes at the top surface of the top block for the cantilever configuration, while the velocity is applied to the entire top block in the double-clamped configuration. The lateral reaction force is obtained at the bottom rigid block, while the lateral displacement is recorded at the top block. The simulation is stopped once the maximum displacement at the top rigid block reaches the net displacement corresponding to each experimental result.
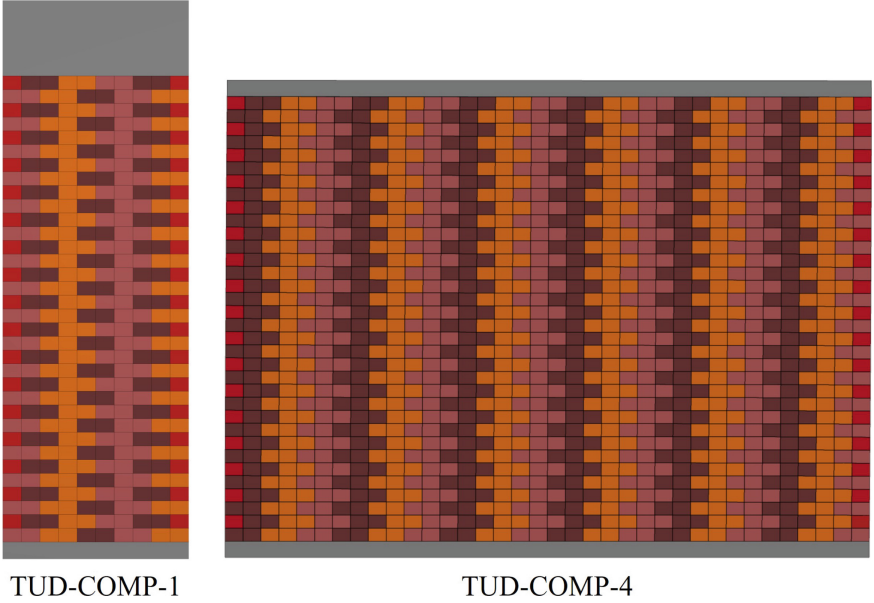
TUD-COMP-1   TUD-COMP-4

**Fig. 4.** Brick discretization of the CS wall test.

4.2   Predicted Structural Performance

In this section, the results of the numerical validations of the four benchmark walls are presented. The global behavior in terms of the force-displacement curve and local behavior in terms of the damage pattern are compared and discussed.

Comparison of Global Behavior The comparison of the force-displacement curves across all four wall models against the experimental envelope curves is presented in Fig. 5. It is important to note that only experimental envelope curves on the loading direction aligned with the numerical simulation are considered in the comparison. In general, the global behavior of the numerically predicted values is in agreement with the experimentally observed responses.

It can be observed, for the slender wall cases, that the numerical model overestimated the maximum observed base shear compared to the experimental responses. The TUD-COMP-0a model predicted the maximum peak load within 20% of the experimentally observed value, while the peak load predicted by the TUD-COMP-1 model was 40% higher compared to the experimental results. However, similar to the experimentally observed behavior, both slender wall models exhibited a ductile response with force degradation observed at the later stage of the analysis for the TUD-COMP-0a model, while no force degradation occurred on the TUD-COMP-1 model until the end of the analysis.

It is important to highlight that even though the numerical response of TUD-COMP-0a overestimated the experimentally observed envelope curve in the positive direction (the direction that aligned with the numerical loading direction),

**(a)** Slender walls   **(b)** Squat walls
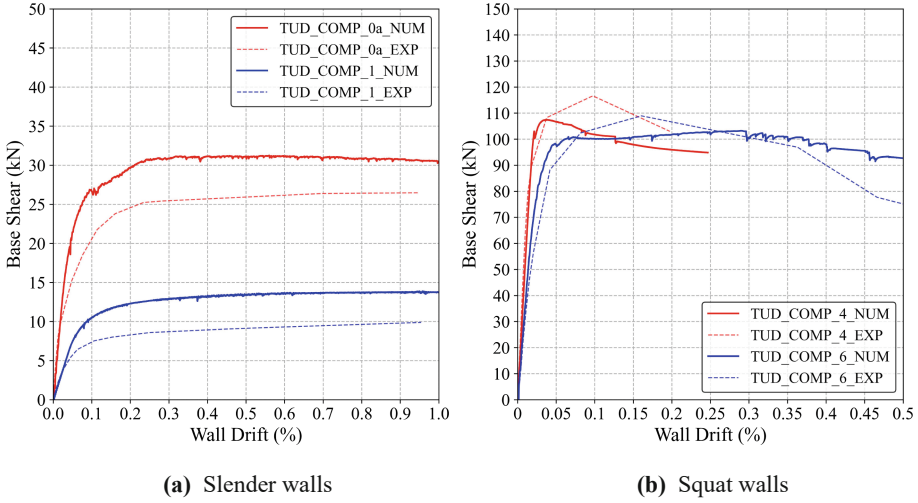
Fig. 5. Comparison experimental and numerical force-displacement curves.

the numerical force-displacement response underestimated the envelope curve in the negative direction, indicating the asymmetric response of the experimental TUD-COMP-0a specimen. This shows that the accumulation of damage during cyclic loading in one direction could affect the behavior in the other direction.

Furthermore, while the peak load was also overestimated for the case of TUD-COMP-1, it has been reported in Messali et al. [9] that the measured peak load of TUD-COMP-1 wall specimen was considerably lower than the predicted values from analytical and numerical simulations. It was also reported in the experimental findings that in the subsequent test of TUD-COMP-2 with the same aspect ratio and boundary condition, the observed peak load was only 15% lower than TUD-COMP-1 even though the vertical pre-compression stress was 28.5% lower.

In contrast to the slender wall specimens, the peak shear load observed in the squat wall specimens was considerably higher, but the squat walls failed at a smaller drift when compared to the slender wall specimens. The numerical force-displacement response of the squat wall models predicted by the proposed modeling strategy was also in good agreement with the experimentally observed responses with strength degradation observed after the peak capacity was reached. While both slender wall models overestimated the experimentally observed peak capacity, both squat wall models underestimated the peak capacity with less than 10% relative error. Nevertheless, it can be seen that the global behavior of the experimental wall specimens was predicted by the numerical model with an acceptable accuracy.

Comparison of Local Behavior The numerically predicted crack patterns of all wall models at the end of the analysis are presented in Fig. 6. The crack pattern was magnified 30 times, with the undeformed configuration shown in

TUD-COMP-0a   TUD-COMP-4

TUD-COMP-1   TUD-COMP-6
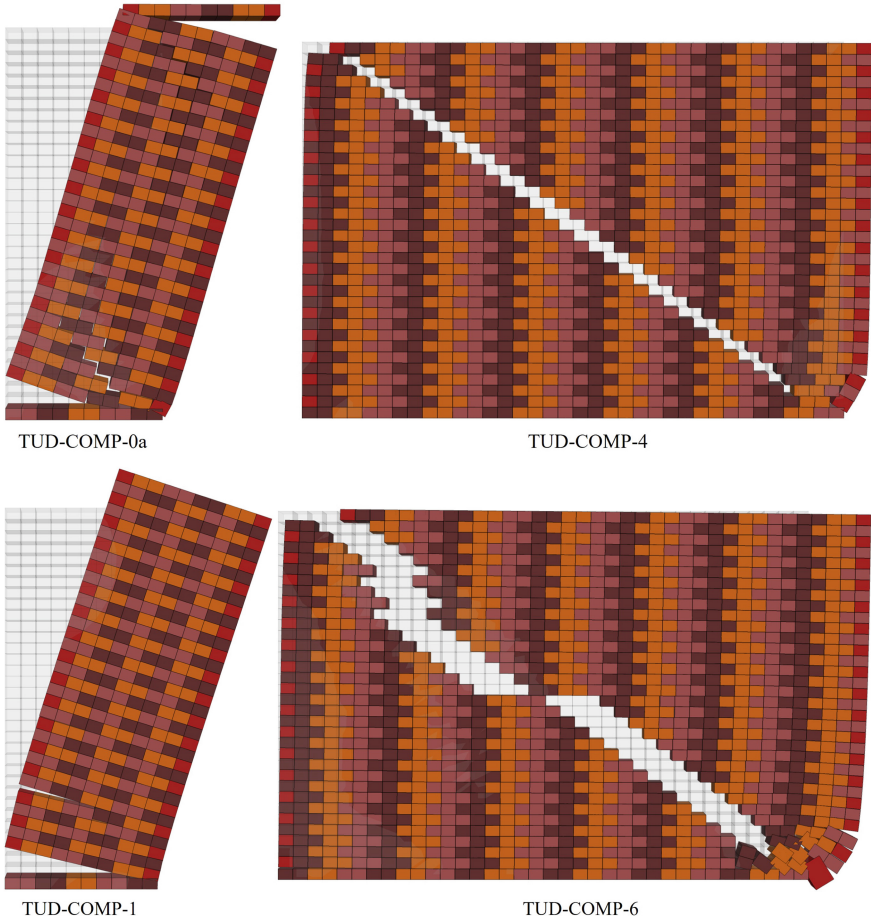
Fig. 6. Crack pattern of the models at the end of the analysis (Def factor: 30).

grey shading, for better visualization. It is evident from the numerical crack patterns that the predicted local behaviors of all models were in good agreement with the experimentally observed crack patterns, shown in Fig. 2.

For the double-clamped slender wall model (TUD-COMP-0a), it is clear that a diagonal shear crack opened at the bottom section of the wall model and propagated from one corner to the other. Furthermore, flexural cracks that opened from one end to the other occurred at the top-most course of the wall model, which also existed in the experimentally observed crack pattern. Crushing of the compressed toe was observed at the top-left and bottom-right sections of the wall, visualized in the form of block interpenetration in Fig. 6.

The localization of the damage in the double-clamped squat wall model (TUD-COMP-4) was also in relatively good agreement with the experimentally observed response. The diagonal shear crack opened and localized in one major

diagonal crack until the end of the analysis. No splitting of the brick units was found along the diagonal crack, which was consistent with the experimental findings. Toe crushing was observed at the bottom right corner of the wall model at the later stage of the analysis.

The damage pattern in the cantilever slender wall of TUD-COMP-1 was slightly different compared to the experimental response, where three flexural cracks occurred at the bottom section of the wall with no occurrence of diagonal cracks. However, consistent with the experimental response, no flexural cracks were found at the top section of the wall model.

Finally, the damage pattern in the cantilever squat wall model of TUD-COMP-6 was somewhat in good agreement with that observed in the experiment. In contrast with the double-clamped model of TUD-COMP-4, the diagonal crack was slightly dispersed with several splitting of the brick units at the bottom-right corner of the wall close to the compressed toes. Further dispersion of the diagonal cracks into multiple cracks was determined in the experiment due to the cyclic loading condition and could, therefore, not be captured via the monotonic loading condition imposed on the numerical simulation. Toe crushing was also observed at the bottom-right corner of the wall, represented as block interpenetration.

With the lateral velocity of 1.0mm s^{-1} and the average tetrahedral aspect ratio (ratio of shortest edge-length to longest edge-length) of 0.61, the required timestep to achieve stability for all models was set at 3.6×10^{-6}. The total elapsed time for the squat wall models was 3 days using the commercial Windows laptop with a 2.6 GHz Intel Core i9 processor and 32 GB of memory. Meanwhile, the total elapsed time for the slender wall models was 5 days using a Windows workstation with a 3.2 GHz Intel Xeon processor and 512 GB of memory. The elapsed time was longer in the slender wall models since the wall drift was larger compared to the squat wall models.

It is clear that the numerical modeling strategy lacks computational efficiency with regard to the time required to complete the analysis, as the explicit time-marching integration scheme was conditionally stable depending on the time steps required to achieve stability. However, it is also important to note that in contrast to the implicit-based numerical simulations, the DEM framework was able to conduct the whole analysis in one run without any intervention in between the simulations due to convergence issues or numerical instabilities. Therefore, the stopping criterion also needs to be properly defined by the modelers, e.g. by imposing a limiting displacement that stops the analysis when the maximum displacement of the system reaches the limit.

5   Conclusions

In this paper, a robust contact constitutive model recently proposed by the authors within the simplified micro-modeling approach using the distinct element method (DEM) is adopted to simulate the structural response of unreinforced masonry (URM) walls subjected to in-plane shear-compression loading. The constitutive model uses a multi-surface plasticity concept with damage mechanics to

account for the tension, shear, compression, and mixed modes failure. Piecewise linear softening functions are used to define the post-peak degradation in tensile and shear regimes, while the hardening/softening function is implemented in the compressive regime.

The proposed contact model is used to simulate a set of experiments on calcium-silicate walls subjected to pre-compression and cyclic in-plane lateral loads with different aspect ratios and boundary conditions. The global behavior in terms of the force-displacement curve simulated by the numerical models was in good agreement with the experimentally obtained curve, even though the experimental peak load was overestimated in the slender wall models and underestimated in the squat wall models. The local behavior in terms of predicted failure mechanisms also matched those from the experiments with localization of the crack pattern clearly represented in the numerical models. Even though the robustness is clear in terms of the fact that convergence issues and numerical instabilities are alleviated in the explicit integration scheme, the computational efficiency in terms of elapsed time could still be improved.

The proposed numerical modeling strategy is just the first stage of the implementation of the contact model for masonry structures within the DEM framework. Refinements of this model will include the stiffness degradation in the unit-mortar interfaces and potential crack surfaces of the brick units to accommodate the behavior of masonry structures when subjected to cyclic loading and the study of the variability of material properties to assess the stochastic nature of masonry structures.

References

1. Addessi D, Sacco E, Paolone A (2010) Cosserat model for periodic masonry deduced by nonlinear homogenization. Eur J Mech A/Solids 29(4):724–737
2. Bui TT, Limam A, Sarhosis V, Hjiaj M (2017) Discrete element modelling of the in-plane and out-of-plane behaviour of dry-joint masonry wall constructions. Eng Struct 136:277–294
3. D'Altri AM, de Miranda S, Castellazzi G, Sarhosis V (2018) A 3D detailed micro-model for the in-plane and out-of-plane numerical analysis of masonry panels. Comput Struct 206:18–30
4. Gaetano D, Greco F, Leonetti L, Lonetti P, Pascuzzo A, Ronchei C (2022) An interface-based detailed micro-model for the failure simulation of masonry structures. Eng Failure Anal 142:1–22
5. Jafari S, Rots JG, Esposito R (2019) Core testing method to assess nonlinear behavior of brick masonry under compression: a comparative experimental study. Construct Build Mater 218:193–205
6. Kumar N, Barbato M (2019) New constitutive model for interface elements in finite-element modeling of masonry. J Eng Mech 145(5):1–15
7. Lourenço PB, Rots JG (1997) Multisurface interface model for analysis of masonry structures. J Eng Mech 123(7):660–668

8. Lourenco P (1996) Computational strategies for masonry structures. Ph.D. thesis, Delft University of Technology
9. Messali F, Esposito R, Ravenshorst G, Rots J (2020) Experimental investigation of the in-plane cyclic behaviour of calcium silicate brick masonry walls. Bull Earthquake Eng 18(8):3963–3994
10. Oktiovan YP, Messali F, Pulatsu B, Lemos JV, Rots JG (2024) A contact-based constitutive model for the numerical analysis of masonry structures using the distinct element method. Comput Struct
11. Pelà L, Cervera M, Roca P (2011) Continuum damage model for orthotropic materials: application to masonry. Comput Methods Appl Mech Eng 200(9–12):917–930
12. Pulatsu B (2023) Coupled elasto-softening contact models in DEM to predict the in-plane response of masonry walls. Comput Particle Mech 10:1759–1770
13. Saloustros S, Pelà L, Cervera M, Roca P (2018) An enhanced finite element macro-model for the realistic simulation of localized cracks in masonry structures: a large-scale application. Int J Archit Heritage 12(3):432–447
14. Sarhosis V, Lemos JV (2018) A detailed micro-modelling approach for the structural analysis of masonry assemblages. Comput Struct 206:66–81
15. Zhang S, Beyer K (2019) Numerical investigation of the role of masonry typology on shear strength. Eng Struct 192:86–102
16. van Zijl G (2004) Modeling masonry shear-compression: role of dilatancy highlighted. J Eng Mech 130(11):1289–1296